



ENVIRONMENTAL DEGRADATION OF ADDITIVELY MANUFACTURED ALLOYS

Improving the Pitting Corrosion Performance of Additively Manufactured 316L Steel Via Optimized Selective Laser Melting Processing Parameters

JOSEPH J. SOPCISAK,¹ MINGXI OUYANG,² DUANE A. MACATANGAY,³
BRENDAN P. CROOM,¹ TIMOTHY J. MONTALBANO,¹
DAVID J. SPROUSTER,² ROBERT G. KELLY,³ JASON R. TRELEWICZ,^{2,4}
RENGASWAMY SRINIVASAN,^{1,5} and STEVEN M. STORCK^{1,6}

1.—Research and Exploratory Development Department, The Johns Hopkins University Applied Physics Laboratory (JHU/APL), Laurel, MD 20723, USA. 2.—Department of Materials Science and Chemical Engineering, Stony Brook University, Stony Brook, NY 11794, USA. 3.—Center for Electrochemical Science and Engineering, Department of Materials Science and Engineering, University of Virginia, Charlottesville, VA 22904, USA. 4.—Institute for Advanced Computational Science, Stony Brook University, Stony Brook, NY 11794, USA. 5.—e-mail: Rengaswamy.Srinivasan@jhuapl.edu. 6.—e-mail: Steven.Storck@jhuapl.edu

Additive manufacturing (AM) has many advantages over conventional manufacturing methods, such as the ability to produce free-form complex shapes and materials with unique properties. Nevertheless, the implementation of AM components into corrosive environments is ultimately limited by the poor corrosion performance of the printed materials when compared to their conventionally manufactured counterparts. In this study, we demonstrate improvement and tailoring of corrosion resistance in AM parts via precise control of laser processing parameters, which were adjusted to optimize pitting corrosion performance for fully dense parts of austenitic stainless steel 316L. Laser power, speed, and hatch spacing were systematically varied while maintaining a constant energy density in a laser powder bed fusion (L-PBF) AM system. Powders were consolidated via selective laser melting (SLM) to establish the parameters influencing pitting performance through potentiostatic anodic oxidation. The results show a strong correlation between processing parameters and resistance to pitting corrosion, attributed to laser velocity-induced variations in microstructure and residual stress state.

INTRODUCTION

The use of additive manufacturing (AM) has grown exponentially in the greater scientific and manufacturing communities due to the ability to make complex parts on-demand with minimal or no post-processing.¹ Metal AM in particular has garnered significant interest as a means to reduce production and storage costs for parts that are highly complex and expensive to produce via conventional manufacturing. One disadvantage of metal AM, however, is the lack of understanding

of the corrosion performance of manufactured parts, which is of the utmost importance in naval and other environments that are highly corrosive or known to promote corrosion. Recent findings indicate that corrosion in AM parts is dictated by their microstructure and associated chemical distribution, which depend on processing conditions.^{2–7} Therefore, a promising path to improve corrosion resistance in metal AM parts is precise control of machine parameters and input materials to tailor the resulting microstructure.

Selective laser melting (SLM) is one of many metal AM methods that can produce dense parts using layer-by-layer laser processing of a metal powder bed in an inert atmosphere.^{8–11} This technique has become very attractive due to its many

(Received December 18, 2021; accepted February 2, 2022;
published online March 11, 2022)

advantages, such as high flexibility of component shape, short processing time, and high dimensional accuracy.¹² Porosity of SLM printed components is dependent on the heating and cooling rates of the melt pool, which trend with the energy input.^{13,14}

$$E = \frac{P}{V \cdot H \cdot t} \quad (1)$$

where E is volumetric energy density in J/mm^3 , P is laser power in W, V is scan velocity in mm/s, H is hatch spacing in mm, and t is layer thickness in mm. This equation incorporates some of the critical parameters for bulk AM deposits and has been used to accurately identify porosity levels.^{15–20}

Stainless steels, and in particular austenitic stainless steels, are an important class of corrosion-resistant alloys with desirable mechanical properties and wide-ranging industrial applications.^{21–23} The corrosion resistance of these alloys is due to the presence of alloyed chromium (16–25%), which allows for the formation of a chromium oxide (Cr_2O_3) surface film on the bulk metal.^{21,24–26} AM of 316L austenitic stainless steel, where the addition of Mo promotes the formation of a more tenacious passive film for improved resistance against pitting and crevice corrosion,²⁷ has been a focus of increasing studies due to the desire for rapid manufacturing of complex, corrosion-resistant components.² The influence of laser processing parameters and their subsequent microstructures on mechanical properties has been widely studied.^{28–39} While there are several studies investigating the corrosion response of SLM 316L,^{3,4,6,7,40–47} a comprehensive evaluation of processing parameters for fully dense parts has yet to be explored from the perspective of improving pitting corrosion. The few studies involving fully dense samples focus on comparing SLM specimens to wrought or other additive techniques;^{48–50} however, they do not investigate the effect of manipulating processing parameters over a broad range in fully dense samples.

Unlike the SLM 316L investigated in this work, the wrought form of 316L has been found to undergo pitting corrosion due to the presence of second phase particles that form from inherent impurities of the steelmaking process, such as MnS. Studies have shown that pitting corrosion initiates around MnS inclusions and attributed to the deficiency of Cr in the austenitic matrix immediately around the MnS particles.^{51–57} The microstructural differences between wrought and SLM 316L have been investigated in regard to the roles that processing plays in corrosion resistance; however, there are many instances of conflicting results in the literature. For example, the lack of MnS has been correlated to an improvement in pitting resistance in SLM specimens in some studies^{40,43} whereas other studies have reported that the presence of pores in SLM specimens lead to a degradation in corrosion

resistance.^{6,58} Since microstructure (including composition) and porosity are both critical variables for corrosion resistance, it is important to quantify both factors independently to fully understand and control the corrosion performance in SLM parts.

This work explores only fully dense or near fully dense material to rule out the role of porosity in corrosion, with a focus on the effect that SLM processing parameters, namely, power, velocity, and hatch spacing, have on pitting corrosion. Varying the processing parameters may impact the microstructural characteristics, therefore in this study, correlations established between processing parameters and corrosion performance are only indirectly related to microstructure. Furthermore, the processing parameters (power, velocity, and hatch spacing) were varied such that the volumetric energy density was maintained at a fixed value of $100 J/mm^3$, which generated fully dense alloy samples. By maintaining a fixed energy density with alloys free of porosity, this work provides new insights into the effect of processing parameters on pitting corrosion independent of defect formation.

EXPERIMENTAL

Materials and Selective Laser Melting

AISI 316L stainless steel powder manufactured by EOS (EOS, Kraling, Germany; EOS art.-no. 9011-0032) with a spherical particle size distribution of 10–53 μm was used in this study; see Table I for the chemical composition provided by EOS. Cylindrical samples 5 mm in height and 16 mm in diameter were manufactured using an EOS M290 DMLS-SLM system, which utilizes a 1060- to 1100-nm, 200-W continuous Yb fiber laser with a fixed 100- μm spot size and an inert argon-purged atmosphere. The layer thickness for all samples was held constant at 20 μm . The volumetric energy density of all the specimens was held constant at $100 J/mm^3$ by systematically adjusting two of the three parameters, as shown in Table II.

Table I. Chemical composition of the 316L powder used in this study

Element	Analysis method	wt%
Fe	–	Balance
Cr	ICP	18.62
Ni	ICP	14.04
Cu	ICP	<.01
Mn	ICP	1.65
Si	ICP	0.37
Mo	ICP	2.77
C	Combustion	.007
S	Combustion	.005
P	ICP	<.010
N	Fusion	.07

Table II. Seven processing parameters used for this 7-sample pitting corrosion study

Condition	Power (W)	Velocity (mm/s)	Hatch (mm)
Control (0)	195	1083	.09
1	234	1300	.09
2	156	866	.09
3	151	1083	.07
4	195	1380	.07
5	240	1083	.11
6	195	885	.11

Two variables were adjusted for processing of each sample in order to hold the volumetric energy density and layer thickness constant across all samples

Porosity Determination

Porosity was quantified for each specimen employing micro-focus x-ray computed tomography (XRCT). XRCT scanning has become a widely used method for characterizing defects and porosity in AM.⁵⁹ The entire volume of each specimen was imaged after being removed from the build plate, prior to any other characterization. All XRCT scans were performed on a North Star Imaging X-50 with a voxel resolution of 13 μm . Data analysis was accomplished in Volume Graphics VGStudio MAX and VGDefX, which employ an automated defect recognition algorithm to compute porosity percentage (per unit volume) of the entire sample.

X-ray Diffraction

To determine the microstructure of the SLM 316L alloy specimens, x-ray diffraction (XRD) measurements were performed at the Pair Distribution Function beamline at the National Synchrotron Light Source-II at the Brookhaven National Laboratory. The sample-to-detector distance, detector tilt, and instrument-based broadening were determined using a NIST LaB₆ powder XRD standard. The x-ray wavelength was 0.1665 Å (74.465 keV) and the sample-to-detector distance was 1231.79 mm. The two-dimensional XRD patterns were corrected by subtracting Kapton and air-scattering components. The TOPAS software package (Bruker) was employed to quantify the lattice parameters and microstructure-based broadening components for each of the specimens (including a modified Williamson–Hall analysis).^{7,60}

Potentiostatic Hold Testing

Each SLM 316L alloy specimen was embedded in slow-cure epoxy, exposing an 8-mm-diameter circular disc as the working electrode (WE). The exposed surface was successively polished to a P1200 grit using SiC paper, cleaned in an ultrasonic bath of deionized water, and mounted in a PAR flat cell holder. Samples were allowed to rest for 90 min in

aqueous 0.6 M NaCl solution (not deaerated) to establish a nearly-stable (less than $\pm 2\text{-mV/min}$ drift) corrosion potential (E_{corr}). All tests were conducted at room temperature ($21^\circ\text{C} \pm 1^\circ\text{C}$).

A three-electrode configuration was employed with a Ag/AgCl/1M KCl reference electrode and a Pt-coil counter electrode. The WE was subject to potentiostatic pulsing from E_{corr} to 1.65 V using a Solartron SI 1287 potentiostat. Although at 1.65 V the alloy experienced anodic oxidation with concomitant evolution of oxygen due to electrolysis of water, the rate of pitting corrosion was observable with minimal interference from crevice corrosion.

Anodic Polarization

Potentiodynamic scans for the Control (0) material were conducted under acidic conditions. The material was polished to P1200-grit with SiC paper. One scan was conducted under reducing conditions with 1 M H₂SO₄ and 0.01 M KSCN. After a 30-min hold under open circuit conditions, the scan was started at 0.05 V below the open circuit potential and anodically scanned to 0.05 V versus SCE.

To investigate the passive–transpassive transition, the potentiodynamic behavior of the Control (0) material in 1 M H₂SO₄ (no thiocyanate) was measured. The material was polished to P1200-grit with SiC prior to testing. After a 30-min OCP hold, the scan began at 0.05 V below the open circuit potential and anodically scanned to 1.2 V versus SCE. Post-test corrosion morphologies for both potentiodynamic tests were characterized by scanning electron microscopy (SEM).

Scanning Electron Microscopy

Corroded SLM 316L surfaces were imaged using SEM to identify preferential attack deriving from the underlying characteristics of the AM microstructures. A Thermo Scientific Scios Dual-BeamTM was used to obtain secondary electron microstructural images.

RESULTS AND DISCUSSION

Porosity Before Potentiostatic Hold

It is clear from prior literature^{3,4,6,40–47} that the effect of porosity on corrosion resistance is critically important to understand when comparisons are drawn regarding the corrosion performance of different samples. In order to reduce the impact of porosity on estimating process parameter effects on corrosion, only fully dense samples were used in this study. Therefore, it is essential to measure and confirm the degree of porosity in each specimen tested for corrosion. Note that most of the porosity data reported in the published literature are based on optical microscopy,⁶¹ sometimes with the assistance of image processing software. Optical microscopy is a two-dimensional imaging technique and thus does not provide porosity data in three dimensions. Archimedes' method is another porosity measuring technique useful in high-porosity materials, but can lead to erroneous results in high-density alloys.⁶²

XRCT provides accurate and quantitative data on volumetric porosity and was thus selected for porosity quantification in our SLM samples. In addition to being completely non-destructive, the three-dimensional datasets allow for a more accurate quantification of porosity, pore-size, shape, and spatial distribution, which collectively is of great benefit given the stochastic nature of porosity. Representative XRCT images of two specimens are shown in Fig. 1. All the seven manufacturing conditions described in Table II yielded specimens of similar density (>99.83% dense) when measured at a voxel resolution of 13 μm , with results summarized in Table III.

Potentiostatic Testing

Results from the potentiostatic hold test at 1.65 V are shown in Fig. 2 for all eight current–time records (i–t transients), one for each condition (Table II) plus a wrought sample for comparison. The wrought alloy generally exhibited one of the smallest currents and was resistant to uniform corrosion, but not to pitting and crevice corrosion. The transients for the SLM samples separated into three groups, with Condition 3 exhibiting the highest current, Conditions 2 and 6 the lowest current, and the remaining conditions intermediate currents. On this basis, the latter two conditions were the most resistive to pitting corrosion and consistent with the wrought sample, while Condition 3 was the most susceptible to pitting corrosion. Their resistance to uniform oxidation of the surface cannot be resolved from the i–t transients, due to the inseparability of metal from water oxidation.

Optical Microscopy

The surfaces of the samples were observed under optical microscopy. Figure 3 depicts optical

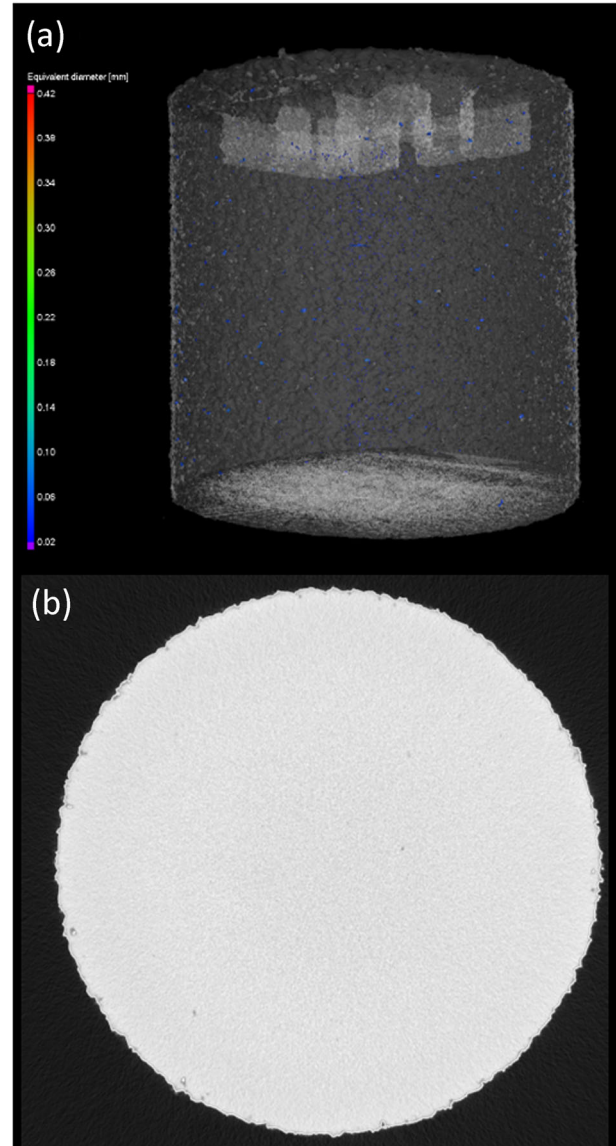


Fig. 1. (a) Representative XRCT scan showing a sample built using Condition #2. This sample is virtually pore-free with a density >99.90% at a voxel resolution of 13 μm , and (b) XRCT cross-section of a sample built with Condition #1 showing a fully dense build. The contrast in the upper image is from the condition number built into each sample.

Table III. Density data acquired via XRCT for all conditions (see Table II) used in this study. Voxel resolution is 13 μm

Condition	Measured density
Control (0)	99.867
1	99.833
2	99.899
3	99.861
4	99.888
5	99.891
6	99.904

micrographs taken before and after the potentiostatic hold (at 1.65 V) test for Condition 1. The as-printed surface revealed no observable surface pores, and damage via pit formation was only detected post-potentiostatic testing. The pre-corrosion surfaces for all samples from Table II were nearly identical to the sample shown in Fig. 3 (left), and, therefore, not reported here.

Figure 4 shows the post-corrosion images from all seven processing conditions; a wrought 316L alloy is included for the purpose of comparison. The surface pits are highlighted in red. The difference in pit density (number of pits per unit area) and pit size varied greatly between samples, with a strong dependency on their processing conditions. The surface of the wrought sample and Condition 3 were among the most pitted, and those of Conditions

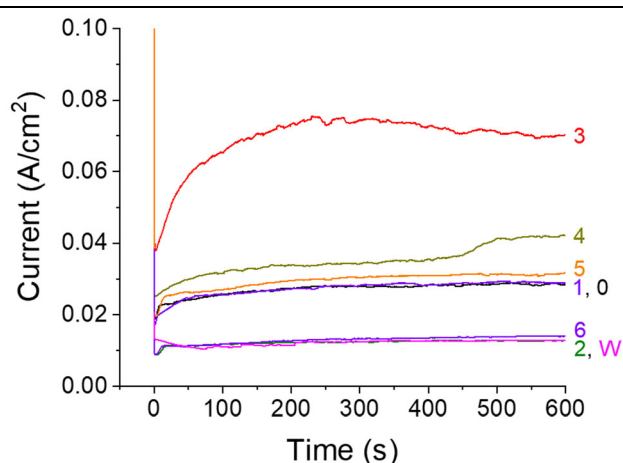


Fig. 2. Current transients measured in 0.6 M NaCl during the potentiostatic hold testing of each of the seven processing conditions at a potential of 1.65V. The behavior of wrought 316L (*W*) is included for reference. Even though E_{corr} was nearly identical for all AM samples, the double layer discharge current and the anodic oxidation current varied widely between the samples, indicating large variations in the adsorption properties and electrode kinetics.

2 and 6 were the least pitted. Conditions 2 and 6 also recorded the smallest currents in potential hold testing (Fig. 2). In contrast, Conditions 1 and 3 generated the largest number of pits, and the former recorded the highest current. There is a distribution of pit density and current amplitude between the samples prepared under the seven processing conditions, highlighting the importance of optimizing build parameters for a component-specific application (in this case, corrosive environments), in addition to material density and mechanical properties.

The wrought 316L exhibited the most crevice corrosion along the perimeter of the exposed surface, consistent with observations reported by others.^{63,64} 316L is also susceptible to crevice corrosion that, under potentiodynamic scanning of ASTM-G61 (0.1667 mV/s scan rate), completely dominates over pitting corrosion. Potential pulsing to far-anodic conditions appeared to help generate more pits and less crevice corrosion, and hence this study adopted a pulse-and-hold at 1.65 V. Almost all the AM samples showed high resistance to crevice corrosion via this method, which may be due to an oxide on the outer surface of the builds.

Corrosion Characteristics and Microstructural Attack

The microstructure of the SLM 316L alloys did not vary to any perceptible degree between the seven processing parameter sets listed in Table II. Figure 5 shows highly-magnified SEM images of corroded Condition 1 (a, c) and Condition 2 (b, d), revealing AM-specific features and corrosion attack along the boundary of the cellular microstructure. Although the most common corrosion morphology in LPBF 316L is preferential attack of the interior of the cellular microstructure,^{6,28,65,66} at the elevated potential used in the present work (+1.65 V(Ag/AgCl)), the boundaries of the cellular structure were

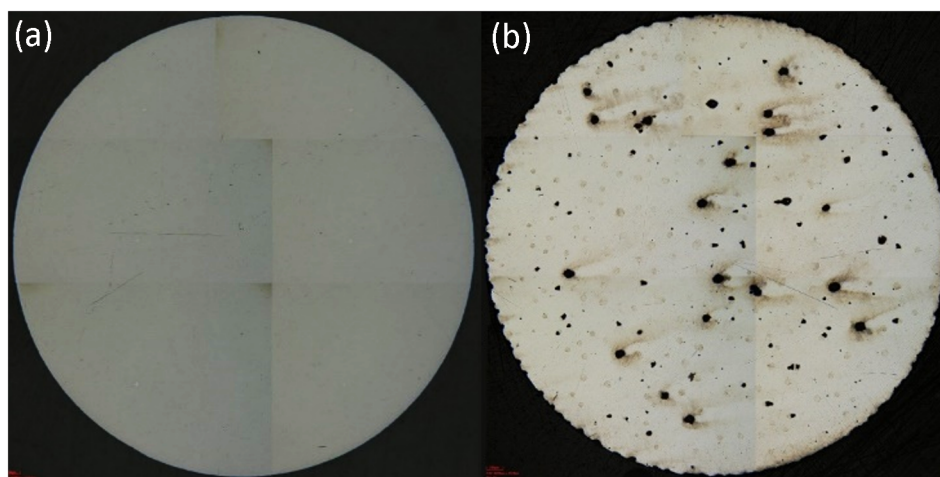


Fig. 3. Optical microscopy of a fully dense sample (Condition 1): as-printed (a) and post-potentiostatic testing (b). The diameter of all the samples was 8 mm.

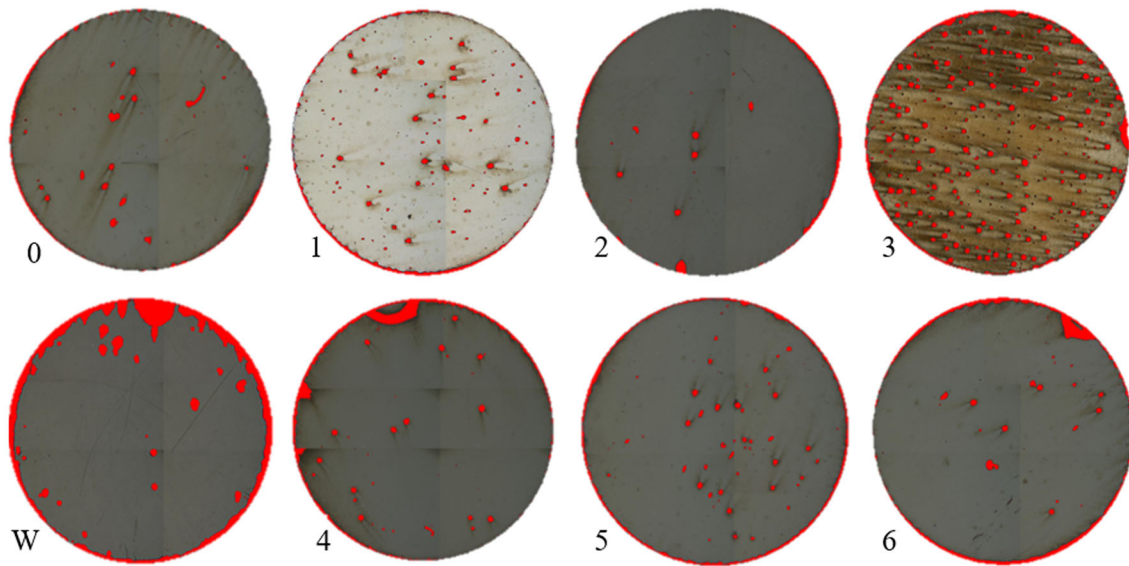


Fig. 4. Resulting surfaces of all 7 processing conditions following potentiostatic hold testing at 1.65 V (*W* wrought). The samples with slower scan speeds (2 and 6) show less pitting corrosion whereas samples with higher scan speeds show an increase in pitting corrosion

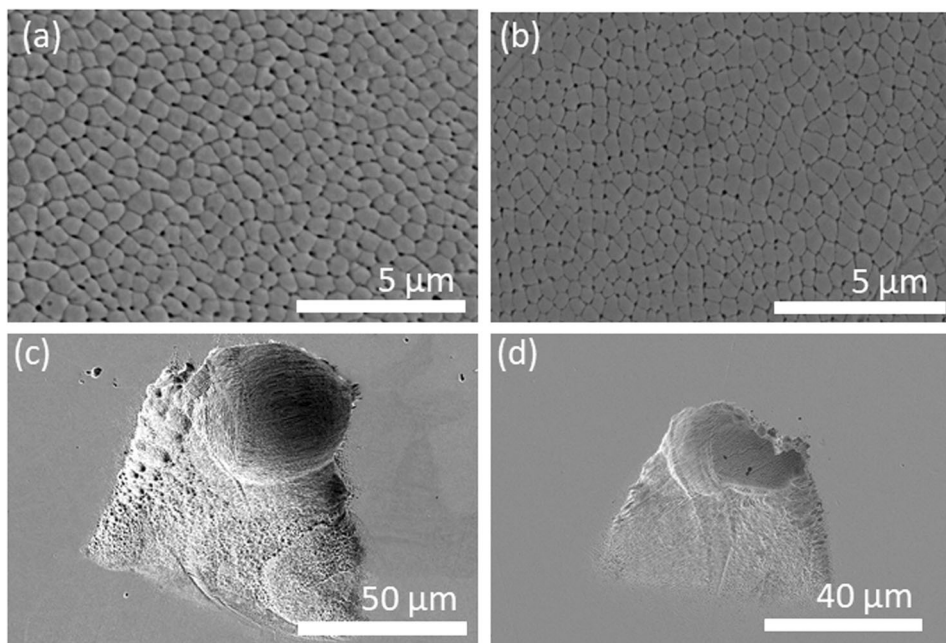


Fig. 5. SEM micrographs showing the localized etching of dislocation cellular walls and representative pits after corrosion testing of Condition 1 (a, c) and Condition 2 (b, d).

preferentially attacked, which has been observed on occasion.^{58,65}

Austenitic stainless steels undergo transpassive dissolution at elevated potentials in which the passive Cr(III)-rich oxide is further oxidized to Cr(VI), which is highly soluble. It has been widely observed that the boundaries of the cellular microstructure are enriched in Cr,^{65,67,68} and that the rate of transpassive dissolution increases with increasing Cr concentration in stainless steels.^{7,65,69,70} Thus, the cellular microstructure boundary attack in Fig. 5 is most likely reflecting

the higher Cr concentration at the boundaries of the cellular microstructure, reported throughout the literature.^{7,69,70} Further evidence of this behavior is shown in Fig. 6, which includes the polarization behavior and resulting corrosion morphologies for the Control sample (0) in 1 M sulfuric acid with or without 0.01 KSCN. In Fig. 6(a), the 0.01 KSCN activates the surface, and the polarization curve shows a dominant active-passive transition. Under these reducing conditions, the interior of the cellular structure is preferentially attacked (Fig. 6(b)) because its lower Cr content renders it more

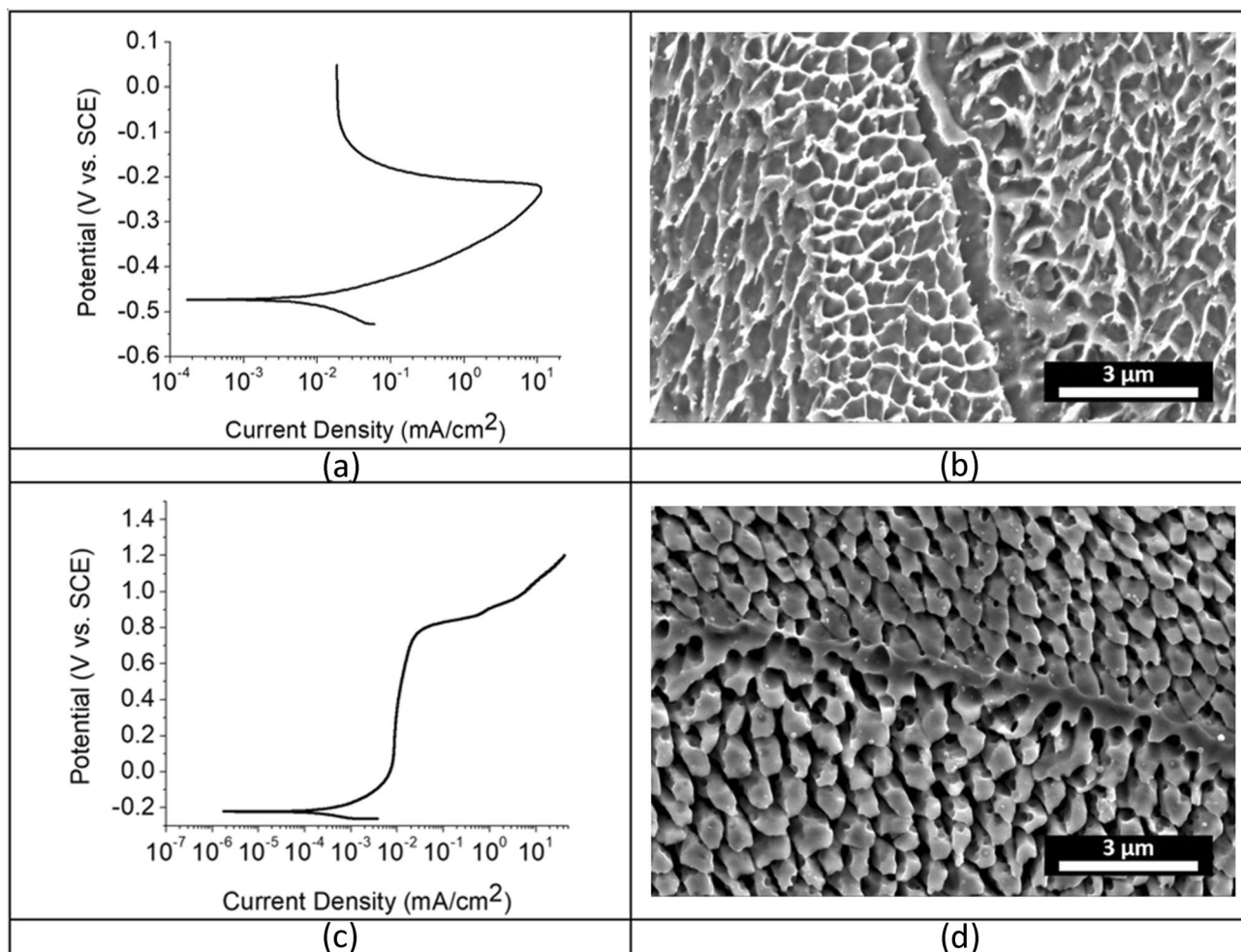


Fig. 6. (a) Polarization curve of the Control sample in 1 M H_2SO_4 + 0.01 KSCN starting 50 mV below the open circuit potential and scanned upwards to 50 mV, versus SCE at a rate of 1.67 mV/s, and (b) the post-test micrograph for this potentiodynamic scan. (c) Polarization curve of the Control sample in 1 M H_2SO_4 starting 50 mV below the open circuit potential and scanned upwards to 1.2 V, versus SCE at a rate of 1.67 mV/s, and (d) the post-test micrograph.

susceptible to active dissolution. In the absence of the 0.01 KSCN, the material is spontaneously passive, and anodic polarization into the transpassive region (Fig. 6(c)) results in preferential attack of the boundaries of the cellular structure (Fig. 6(d)). These data support the suggestion of Cr segregation to the boundaries, although confirmation for these alloys awaits future work. In addition, these data also suggest that the corrosion performance of SLM 316L may not be governed by conventional mechanisms found in wrought materials,⁶³ but is more akin to powder-sintered 316L.⁶⁴

The cellular attack indicates localized corrosion occurring on the length scales that dominate material formation (in the AM process), thereby highlighting the importance of process parameter control. Cellular attack and pitting corrosion were shown to be significantly reduced in Conditions 2 and 6 that were formed under slower laser traverse speeds (Table II). This higher resistance to corrosion in Conditions 2 and 6 can be attributed to the

increasing dwell time (associated with reduced laser traverse speed), resulting in the completion of the alloying process in each layer.^{71,72} Localized chromium concentration at the grain boundaries is known to result in selective attack,⁴¹ as discussed, and the trends observed in this work further support this observation. It is evident from prior literature that reduced traverse speed results in extended liquid lifetime during SLM processing, and in turn improved diffusion of elements during solidification.⁷¹ Therefore, under slower traverse speed, the stoichiometry of the alloy is likely more stabilized, alloying is complete, and elements are less segregated. This results in a robust final product with highly improved corrosion resistance.

Quantitative Microstructural Analysis

Based on the potentiostatic test results and optical microscopy imaging of surface pitting, the Control sample (0) and Condition 2 were investigated by XRD. Condition 2 was selected based on its

combined resistance to anodic oxidation and pitting relative to the other samples with the control serving as the reference. Figure 7(a) shows background-corrected XRD patterns for these two samples with the Miller indices of each reflection labeled for reference. Subtle differences in the peak position and peak full width at half maximum indicated minor microstructure differences, which were quantitatively analyzed by XRD refinements,^{73–77} with the results shown in Fig. 7(b). Both the lattice parameter and dislocation density exhibited an increase with increasing printing speed and consistent with prior reports on 316L produced via SLM.⁷

Higher printing speeds can augment the solidification cooling rates and lead to thermal gradients with an elongated melt pool along the travel direction within a single print track.^{78–80} This has a non-negligible impact on the solidification microstructure and melt pool boundaries,^{80,81} leading to the increase in lattice parameter and dislocation densities. The lattice strain can be ascertained from lattice parameter measurements, as follows:

$$\varepsilon = \frac{a}{a^0} - 1 \quad (2)$$

where a^0 and a represent the stress-free reference lattice parameter and measured lattice parameter, respectively. Based on the XRD analysis of wrought 316L steel, a^0 is 3.595\AA ⁸² while a is determined from Fig. 7(b). With the lattice parameters for both SLM samples greater than the wrought 316L, a quantifiable lattice expansion exists, indicating that the SLM samples do indeed contain quantifiable tensile residual stresses. The larger lattice parameter of the Control sample further suggests that its residual stress will be greater than in Condition C2. Finally, we note that, given the transmission-mode geometry, the lattice parameters are representative

of a through-thickness value. In SLM 316L, residual stresses tend to be compressive near the center of the print and tensile near the surface.^{83,84} Thus, our measurements likely underestimate the surface tensile stress component but nonetheless confirm the presence of tensile residual stresses in the printed samples.

The microstructural analysis presented here has two implications for the pitting behavior. First, increased dislocation densities have been correlated to a reduced pitting potential in pulsed laser AM 316L,⁷ and thus an enhanced susceptibility to pitting. However, the magnitude of the difference in the dislocation densities on these samples is considerably smaller than in the cited study, but with decidedly larger lattice parameters. The corresponding larger tensile residual stress now appears to be non-negligible, whereby the sample containing the reduced tensile residual stress (i.e., Condition 2) exhibits an improved resistance to pitting attack in Fig. 4, consistent with the role of residual stress on metastable pitting behavior in autenitic stainless steels.⁸⁵ While this is an early observation requiring additional understanding of the underlying mechanisms related to passive film integrity in SLM 316L under varying residual stresses, we explore this potential effect in the following section from the perspective of pitting, by further reducing the speed while remaining in the fully dense regime.

Critical Machine Parameters for Optimizing Corrosion Performance

Reduced pitting events were observed in samples with reduced laser velocity. Based on the velocity-dependent residual stresses, it was hypothesized that a reduced laser velocity at constant energy density could result in further resistance against pitting, based on the evidence that the reduced laser

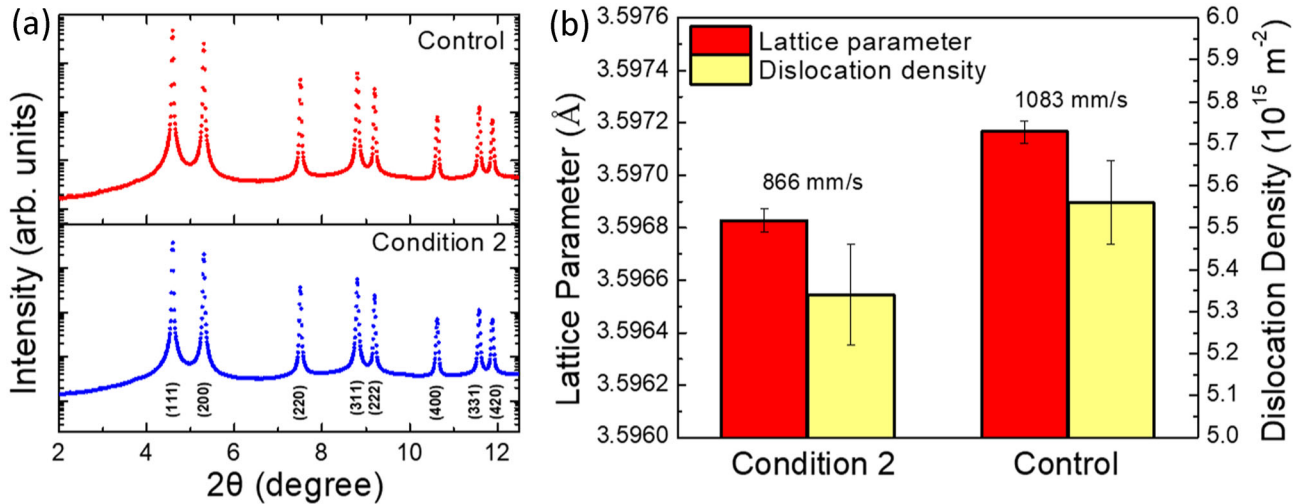


Fig. 7. (a) XRD patterns for SLM 316L Condition 2 relative to the Control sample (0) with FCC reflections indexed for each of the austenite peaks. (b) Quantified microstructural results from XRD refinements on the patterns shown in (a) with printing speed for the two samples included above the respective data columns. The change in lattice parameter indicates differing degrees of tensile residual stress.

velocity is associated with lower residual stresses and a more favorable microstructure (i.e., a reduced dislocation density). Yet another benefit of the reduced laser velocity is the reduction in the cooling rate, which is known to suppress micro-segregation of alloying elements.⁸⁶ These combined attributes of reduced cooling rate and a more uniform microstructure have the potential to reduce surface tensile residual stresses and chemical segregation of Cr common to SLM 316L.

To test this hypothesis, an additional sample was prepared by reducing the print velocity to 722 mm/s while balancing the power to maintain the energy input at 100 J/mm³ akin to the initial study. Results from the potentiostatic hold experiments shown in Fig. 8 demonstrate that the reduction in print velocity to 722 mm/s indeed produces fewer pits, indicative of a higher resistance to pitting corrosion relative to the samples produced at higher speed. This further substantiates that an optimal parameter set for pitting resistance does exist and should be exploited to improve corrosion resistance of AM 316L, while balancing the alloy's density and mechanical behavior.

The main focus of this study has been identifying the relationship between processing parameters (Table II) and corrosion resistance. This study

shows that a 722-mm/s laser velocity combined with 100 J/mm³ input energy results in the best pitting corrosion-resistant AM 316L alloy. A reduced laser velocity is known to produce slower cooling rates, which have been shown to reduce the lattice parameter and dislocation density. It is, however, entirely likely that we have not fully optimized both the laser velocity and the energy input, and that a better distribution of alloying elements and grain/melt pool structures may be achieved through further optimization. Therefore, a large window for innovation exists for further enhancing corrosion resistance in SLM 316L stainless steel.

Finally, it is important to emphasize that the vendor-recommended (control) laser parameters did not result in the best pitting performance (EOS recommended parameters, Control (0) in Table II and Fig. 4). Machine vendors strive to produce fully dense materials with the most stable melt conditions, maximizing strength and elasticity. They may not consider other material characteristics such as corrosion.⁸⁷ However, as processing parameters are optimized for all properties, vendors may adapt them for improved overall performance. While build speed generally represents a critical factor for many applications, considering its impact on manufacturing cost, a slight reduction in processing speed may

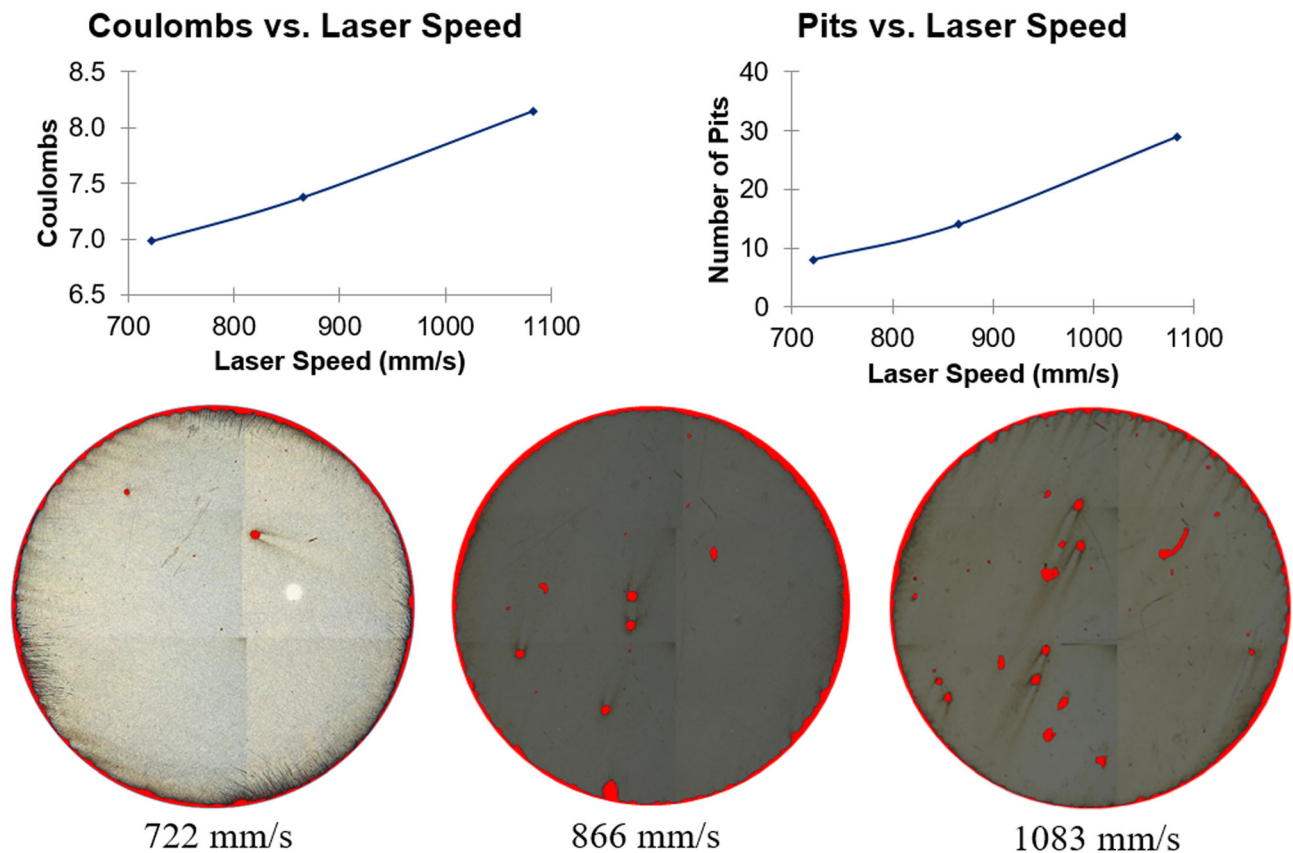


Fig. 8. The benefit of laser speed on corrosion response. A reduced laser velocity produces fewer pits, a higher resistance to corrosion, and lower Coulombs of electricity (in i-t transients) during anodic oxidation. The data points (top), from left to right, correspond to the optical micrographs from left to right (bottom).

be acceptable for achieving dramatic improvements in long-term component durability, especially if that component is difficult to replace in service.

CONCLUSIONS

Multiple samples of 316L were manufactured via SLM by varying the laser processing parameters to determine those that impact pitting corrosion. The present study has revealed a strong correlation between processing parameters and pitting propensity, mostly attributable to laser velocity-induced microstructural variations and residual stress state. A slow laser velocity of 722 mm/s, coupled with 100 J/mm³ input energy, has generated an AM 316L alloy with the greatest resistance to pitting corrosion. Critical parameters for generating corrosion-resistant material while maintaining full or nearly full part density were thus identified through this method. Established connections between processing parameters and corrosion performance is an essential characteristic for additive manufacturing processes, given that printed parts behave very differently than a wrought alloy counterpart and that corrosion is not often considered when vendors develop their recommended machine parameters. These results demonstrate the critical need to tailor AM components and processing for all properties of interest rather than just density and mechanical performance.

ACKNOWLEDGEMENTS

This work was supported by the Office of Naval Research under the Corrosion Control Technologies Program, task order N00024-17-F-8021 under contract N00024-13-D-6400. MO, DJS, and JRT acknowledge support from the same program but under contract N00014-20-1-2293. D.M. and R.K. gratefully acknowledge the support from the Office of Naval Research, Contract No. N00014-17-1-2533 (Dr. Airan Perez, Program Manager). The authors would like to thank Dr. Morgan Trexler and Dr. Jeffrey Maranchi for their program management efforts at JHU/APL. The authors would also like to thank Christopher M. Peitsch, Jarod C. Gagnon, Christopher M. Barr, and Lina Valivullah for their contributions to this work. This research used the Pair Distribution Function Beamline of the National Synchrotron Light Source II, a U.S. Department of Energy (DOE) Office of Science User Facility operated for the DOE Office of Science by Brookhaven National Laboratory under Contract No. DE-SC0012704.

REFERENCES

1. P. Kocovic, *3D Printing and Its Impact on the Production of Fully Functional Components: Emerging Research and Opportunities: Emerging Research and Opportunities* (IGI Global, Hershey, 2017).
2. G. Sander, J. Tan, P. Balan, O. Gharbi, D. Feenstra, L. Singer, S. Thomas, R. Kelly, J.R. Scully, and N. Birbilis, *Corrosion* 74, 1318–1350. (2018).

3. X. Ni, D. Kong, W. Wu, L. Zhang, C. Dong, B. He, L. Lu, K. Wu, and D. Zhu, *J. Mater. Eng. Perform.* 27, 3667–3677. (2018).
4. M. Laleh, A.E. Hughes, W. Xu, N. Haghdadi, K. Wang, P. Cizek, I. Gibson, and M.Y. Tan, *Corros. Sci.* 161, 108189. (2019).
5. A. Hemmasian Etefagh, S. Guo, and J. Raush, *Addit. Manuf.* 37, 101689. <https://doi.org/10.1016/j.addma.2020.10.1689> (2021).
6. J.R. Trelewicz, G.P. Halada, O.K. Donaldson, and G. Manogharan, *JOM* 68, 850–859. (2016).
7. D.J. Sprouster, W. Streit Cunningham, G.P. Halada, H. Yan, A. Pattammattel, X. Huang, D. Olds, M. Tilton, Y.S. Chu, E. Dooryhee, G.P. Manogharan, and J.R. Trelewicz, *Addit. Manuf.* 47, 102263. <https://doi.org/10.1016/j.addma.2021.102263> (2021).
8. D. Herzog, V. Seyda, E. Wycisk, and C. Emmelmann, *Acta Mater.* 117, 371–392. <https://doi.org/10.1016/j.actamat.2016.07.019> (2016).
9. E.T. Akinlabi, R.M. Mahamood, and S.A. Akinlabi, *Advanced Manufacturing Techniques Using Laser Material Processing* (IGI Global, Pennsylvania, 2016).
10. D. Pham, and S.S. Dimov, *Rapid Manufacturing: The Technologies and Applications of Rapid Prototyping and Rapid Tooling* (Springer, Berlin, 2012).
11. P.K. Gokuldoss, S. Kolla, and J. Eckert, *Materials* 10, 672. (2017).
12. W.J. Sames, F. List, S. Pannala, R.R. Dehoff, and S.S. Babu, *Int. Mater. Rev.* 61, 315–360. (2016).
13. V. Shapovalov, *MRS Bull.* 19, 24–28. (1994).
14. K. Prashanth, S. Scudino, T. Maity, J. Das, and J. Eckert, *Mater. Res. Lett.* 5, 386–390. (2017).
15. M. Guo, D. Gu, L. Xi, H. Zhang, J. Zhang, J. Yang, and R. Wang, *Int. J. Refract. Metals Hard Mater.* 84, 105025. <https://doi.org/10.1016/j.jrmhm.2019.105025> (2019).
16. M. Ghayoor, K. Lee, Y. He, C.-H. Chang, B.K. Paul, and S. Pasebani, *Addit. Manuf.* 32, 101011. <https://doi.org/10.1016/j.addma.2019.101011> (2020).
17. K. Moussaoui, W. Rubio, M. Mousseigne, T. Sultan, and F. Rezaei, *Mater. Sci. Eng. A* 735, 182–190. <https://doi.org/10.1016/j.msea.2018.08.037> (2018).
18. T. Montalbano, B. Briggs, J. Waterman, S. Nimer, C. Peitsch, J. Sopcisak, D. Trigg and S. Storck, *J. Mater. Process. Technol.* (in review) (2020).
19. D. Clymer, J. Cagan, and D. Beuth, *J. Mech. Design.* <http://doi.org/10.1115/1.4037302> (2017).
20. J.V. Gordon, S.P. Narra, R.W. Cunningham, H. Liu, H. Chen, R.M. Suter, J.L. Beuth, and A.D. Rollett, *Addit. Manuf.* 36, 101552. <https://doi.org/10.1016/j.addma.2020.10.1552> (2020).
21. A.J. Sedriks, *Corrosion of Stainless Steels*. 2nd Edn, (Wiley-Interscience, New York, 1996).
22. L. Vitos, P.A. Korzhavyi, and B. Johansson, *Phys. Rev. Lett.* 88, 155501. (2002).
23. M. Sumita, T. Hanawa, and S. Teoh, *Mater. Sci. Eng. C* 24, 753–760. (2004).
24. M.F. McGuire, *Stainless Steels for Design Engineers* (ASM International, Russell Township, 2008).
25. J.R. Davis, *Stainless Steels* (ASM International, Russell Township, 1994).
26. A. Al-Amr, *Mechanical behavior and structure of passive films on austenitic stainless steels* (2005).
27. A. Pardo, M.C. Merino, A.E. Coy, F. Viejo, R. Arrabal, and E. Matykina, *Corros. Sci.* 50, 1796–1806. <https://doi.org/10.1016/j.corsci.2008.04.005> (2008).
28. E. Liverani, S. Toschi, L. Ceschini, and A. Fortunato, *J. Mater. Process. Technol.* 249, 255–263. (2017).
29. J. Suryawanshi, K. Prashanth, and U. Ramamurty, *Mater. Sci. Eng. A* 696, 113–121. (2017).
30. A. Deev, P. Kuznetsov, and S. Petrov, *Phys. Procedia* 83, 789–796. (2016).
31. M.L. Montero-Sistiaga, M. Godino-Martinez, K. Boschmans, J.-P. Kruth, J. Van Humbeeck, and K. Vanmeensel, *Addit. Manuf.* 23, 402–410. (2018).

32. T. Larimian, M. Kannan, D. Grzesiak, B. AlMangour, and T. Borkar, *Mater. Sci. Eng. A* 770, 138455. (2020).
33. Z. Wang, T.A. Palmer, and A.M. Beese, *Acta Mater.* 110, 226–235. (2016).
34. P. Zhang, and Z. Liu, *Mater. Des.* 100, 254–262. (2016).
35. T. LeBrun, T. Nakamoto, K. Horikawa, and H. Kobayashi, *Mater. Des.* 81, 44–53. (2015).
36. A. Yadollahi, N. Shamsaei, S.M. Thompson, and D.W. Seely, *Mater. Sci. Eng. A* 644, 171–183. (2015).
37. K. Saeidi, X. Gao, F. Lofaj, L. Kvetková, and Z.J. Shen, *J. Alloys Compd.* 633, 463–469. (2015).
38. K. Saeidi, X. Gao, Y. Zhong, and Z.J. Shen, *Mater. Sci. Eng. A* 625, 221–229. (2015).
39. Z. Sun, X. Tan, S.B. Tor, and W.Y. Yeong, *Mater. Des.* 104, 197–204. (2016).
40. Q. Chao, V. Cruz, S. Thomas, N. Birbilis, P. Collins, A. Taylor, P.D. Hodgson, and D. Fabijanic, *Scr. Mater.* 141, 94–98. (2017).
41. D. Macatangay, S. Thomas, N. Birbilis, and R. Kelly, *Corrosion* 74, 153–157. (2018).
42. D. Kong, X. Ni, C. Dong, X. Lei, L. Zhang, C. Man, J. Yao, X. Cheng, and X. Li, *Mater. Des.* 152, 88–101. (2018).
43. G. Sander, S. Thomas, V. Cruz, M. Jurg, N. Birbilis, X. Gao, M. Brameld, and C. Hutchinson, *J. Electrochem. Soc.* 164, C250–C257. (2017).
44. Y. Sun, A. Moroz, and K. Alrbaey, *J. Mater. Eng. Perform.* 23, 518–526. (2014).
45. K. Geenen, A. Röttger, and W. Theisen, *Mater. Corros.* 68, 764–775. (2017).
46. C. Man, Z. Duan, Z. Cui, C. Dong, D. Kong, T. Liu, S. Chen, and X. Wang, *Mater. Lett.* 243, 157–160. <https://doi.org/10.1016/j.matlet.2019.02.047> (2019).
47. Z. Duan, C. Man, C. Dong, Z. Cui, D. Kong and X. Wang, *Corros. Sci.* 108520 (2020).
48. C. Man, C. Dong, T. Liu, D. Kong, D. Wang, and X. Li, *Appl. Surf. Sci.* 467, 193–205. (2019).
49. A.B. Kale, B.-K. Kim, D.-I. Kim, E. Castle, M. Reece, and S.-H. Choi, *Mater. Character.* 163, 110204. (2020).
50. D. Kong, C. Dong, X. Ni, L. Zhang, H. Luo, R. Li, L. Wang, C. Man, and X. Li, *Appl. Surf. Sci.* 504, 144495. (2020).
51. M.P. Ryan, D.E. Williams, R.J. Chater, B.M. Hutton, and D.S. McPhail, *Nature* 415, 770–774. (2002).
52. D.E. Williams, M.R. Kilburn, J. Cliff, and G.I. Waterhouse, *Corros. Sci.* 52, 3702–3716. (2010).
53. M. Baker, and J. Castle, *Corros. Sci.* 34, 667–682. (1993).
54. T.S.L. Wijesinghe, and D.J. Blackwood, *Corros. Sci.* 49, 1755–1764. (2007).
55. J. Jun, K. Holguin, and G. Frankel, *Corrosion* 70, 146–155. (2014).
56. Q. Meng, G. Frankel, H. Colijn, and S. Goss, *Nature* 424, 389–390. (2003).
57. R. Lillard, M. Kashfipour, and W. Niu, *J. Electrochem. Soc.* 163, C440–C451. (2016).
58. R.F. Schaller, A. Mishra, J.M. Rodelas, J.M. Taylor, and E.J. Schindelholz, *J. Electrochem. Soc.* 165, C234. (2018).
59. H. Villarraga-Gómez, C.M. Peitsch, A. Ramsey and S.T. Smith, In *2018 ASPE and euspen Summer Topical Meeting: Advancing Precision in Additive Manufacturing*, (Lawrence Berkeley National Laboratory Berkeley, California: 2018, pp 201–209).
60. D.J. Sprouster, J. Sinsheimer, E. Dooryhee, S.K. Ghose, P. Wells, T. Stan, N. Almirall, G.R. Odette, and L.E. Ecker, *Scr. Mater.* 113, 18–22. <https://doi.org/10.1016/j.scriptamat.2015.10.019> (2016).
61. A.B. Spierings, M. Schneider and R. Eggenberger, *Rapid Prototyping J.* (2011).
62. J.A. Slotwinski, E.J. Garboczi, and K.M. Hebenstreit, *J. Res. Nat. Inst. Stand. Technol.* 119, 494. (2014).
63. B. Cai, Y. Liu, X. Tian, F. Wang, H. Li, and R. Ji, *Corros. Sci.* 52, 3235–3242. <https://doi.org/10.1016/j.corsci.2010.05.040> (2010).
64. B.S. Kargar, M.H. Moayed, A. Babakhani, and A. Davoodi, *Corros. Sci.* 53, 135–146. <https://doi.org/10.1016/j.corsci.2010.09.004> (2011).
65. Y. Hwa, C.S. Kumai, N. Yang, J.K. Yee, and T.M. Devine, *Corrosion* 77, 1014–1024. <https://doi.org/10.5006/3779> (2021).
66. Y. Cui, and C.D. Lundin, *Mater. Design* 28, 324–328. <http://doi.org/10.1016/j.matdes.2005.05.022> (2007).
67. Y. Zhong, L. Liu, S. Wikman, D. Cui, and Z. Shen, *J. Nuclear Mater.* 470, 170–178. <https://doi.org/10.1016/j.jnucmat.2015.12.034> (2016).
68. S. Gao, Z. Hu, M. Duchamp, P.S.S.R. Krishnan, S. Tekumalla, X. Song, and M. Seita, *Acta Mater.* 200, 366–377. <https://doi.org/10.1016/j.actamat.2016.09.015> (2020).
69. M. Ziętała, T. Durejko, M. Polański, I. Kunce, T. Płociński, W. Zieliński, M. Łazińska, W. Stępniewski, T. Czujko, K.J. Kurzydłowski, and Z. Bojar, *Mater. Sci. Eng. A* 677, 1–10. <https://doi.org/10.1016/j.msea.2016.09.028> (2016).
70. Y.M. Wang, T. Voisin, J.T. McKeown, J. Ye, N.P. Caltà, Z. Li, Z. Zeng, Y. Zhang, W. Chen, T.T. Roehling, R.T. Ott, M.K. Santala, P.J. Depond, M.J. Matthews, A.V. Hamza, and T. Zhu, *Nat. Mater.* <https://doi.org/10.1038/nmat5021> (2017).
71. Q. Shi, D. Gu, M. Xia, S. Cao, and T. Rong, *Opt. Laser Technol.* 84, 9–22. (2016).
72. Y. Li, K. Zhou, S.B. Tor, C.K. Chua, and K.F. Leong, *Int. J. Heat Mass Transf.* 108, 2408–2416. (2017).
73. L. McCusker, R. Von Dreele, D. Cox, D. Louër, and P. Scardi, *J. Appl. Crystallogr.* 32, 36–50. (1999).
74. P. Scardi, C.L. Azanza Ricardo, C. Perez-Demydenko, and A.A. Coelho, *J. Appl. Crystallogr.* 51, 1752–1765. (2018).
75. T. Shintani, and Y. Murata, *Acta Mater.* 59, 4314–4322. <https://doi.org/10.1016/j.actamat.2011.03.055> (2011).
76. T. Simm, P. Withers, and J.Q. da Fonseca, *Mater. Des.* 111, 331–343. (2016).
77. T. Ungár, A.D. Stoica, G. Tichy, and X.-L. Wang, *Acta Mater.* 66, 251–261. (2014).
78. S. Bontha, N.W. Klingbeil, P.A. Kobryn, and H.L. Fraser, *Mater. Sci. Eng. A* 513, 311–318. (2009).
79. P. Promopattum, S.-C. Yao, P.C. Pistorius, and A.D. Rollett, *Engineering* 3, 685–694. (2017).
80. Y. Lee, and W. Zhang, *Addit. Manuf.* 12, 178–188. (2016).
81. J. Gockel, L. Sheridan, S.P. Narra, N.W. Klingbeil, and J. Beuth, *JOM* 69, 2706–2710. (2017).
82. Y. Nishihara, Y. Nakajima, A. Akashi, N. Tsujino, E. Takahashi, K.-I. Funakoshi, and Y. Higo, *Am. Miner.* 97, 1417–1420. (2012).
83. P. Mercelis, and J.P. Kruth, *Rapid Prototyping J.* 12, 254–265. <https://doi.org/10.1108/13552540610707013> (2006).
84. A.S. Wu, D.W. Brown, M. Kumar, G.F. Gallegos, and W.E. King, *Metall. Mater. Trans. a-Phys. Metall. Mater. Sci.* 45A, 6260–6270. <https://doi.org/10.1007/s11661-014-2549-x> (2014).
85. L. Guan, J. Cai, X. Yang, Y. Li, and G. Wang, *Mater. Corrosion* 71, 537–542. <https://doi.org/10.1002/maco.201911304> (2020).
86. Y. Wang, and J. Shi, *Procedia Manuf.* 26, 941–951. <https://doi.org/10.1016/j.promfg.2018.07.121> (2018).
87. E.G.-E.O. Systems, and E.O.S. Company, *HHE* 05, 2014. (2019).